

A recursive neural-network-based subgrid-scale model for large eddy simulation: application to homogeneous isotropic turbulence

Chonghyuk Cho¹, Jonghwan Park¹ and Haecheon Choi^{1,2†}

¹Department of Mechanical Engineering, Seoul National University, Seoul 08826, Republic of Korea

²Institute of Advanced Machines and Design, Seoul National University, Seoul 08826, Republic of Korea

(Received xx; revised xx; accepted xx)

We introduce a novel recursive process to a neural-network-based subgrid-scale (NN-based SGS) model for large eddy simulation (LES) of high Reynolds number turbulent flow. This process is designed to allow an SGS model to be applicable to a hierarchy of different grid sizes without requiring an expensive filtered direct numerical simulation (DNS) data: 1) train an NN-based SGS model with filtered DNS data at a low Reynolds number; 2) apply the trained SGS model to LES at a higher Reynolds number; 3) update this SGS model with training data augmented with filtered LES (fLES) data, accommodating coarser filter size; 4) apply the updated NN to LES at a further higher Reynolds number; 5) go back to 3) until a target (very coarse) filter size divided by the Kolmogorov length scale is reached. We also construct an NN-based SGS model using a dual NN architecture whose outputs are the SGS normal stresses for one NN and the SGS shear stresses for the other NN. The input is composed of the velocity gradient tensor and grid size. Furthermore, for the application of an NN-based SGS model trained with one flow to another flow, we modify the NN by eliminating bias and introducing leaky rectified linear unit function as an activation function. The present recursive SGS model is applied to forced homogeneous isotropic turbulence (FHIT), and successfully predicts FHIT at high Reynolds numbers. The present model trained from FHIT is also applied to decaying homogeneous isotropic turbulence, and shows an excellent prediction performance.

1. Introduction

Large eddy simulation (LES) is an effective tool for predicting turbulent flow because it does not require significant computational resources towards resolution of smaller eddies. This resource reduction is realized through modeling of eddy motions at scales smaller than the grid size (called subgrid scales). The subgrid-scale (SGS) stress from these SGS motions should be modeled to close the governing equations for LES.

The SGS models have been derived for decades based on turbulence theory and statistical approximation. A subset of these models that favor simplicity and stability are represented as linear eddy-viscosity models. Examples include the Smagorinsky model (Smagorinsky 1963), based on the theory that the rate of energy transfer to smaller eddies is counterbalanced by the viscous dissipation within the inertial subrange, WALE

† Email address for correspondence: choi@snu.ac.kr.

model (Nicoud & Ducros 1999), using square of the velocity gradient tensor and analyzing proper near-wall scaling for the eddy viscosity, and Vreman model (Vreman 2004), rooted in the principle that the SGS stress should be reduced in near-wall region or vanish in laminar flow. Many authors started by Germano *et al.* (1991) have adopted dynamic approaches to extend eddy-viscosity models to more intricate flows. Scale-similarity model (SSM) (Bardina *et al.* 1980) assumed that the interplay between resolved and modeled eddies can be accurately delineated by the difference between the filtered and doubly filtered velocities. Lastly, gradient model (GM) (Clark *et al.* 1979) was derived through an approximation technique that employed the Taylor expansion of box filtering. Nevertheless, these models contain some limitations. The linear eddy-viscosity models, in particular, show very low correlations with true SGS stresses in *a priori* tests, irrelevant to the implementation of a dynamic approach, while they work adequately in actual simulations (Liu *et al.* 1994; Salvetti & Banerjee 1995; Park *et al.* 2005). In contrast, both SSM and GM exhibit improved results in *a priori* tests, but they do not sufficiently dissipate turbulent kinetic energy in actual simulations, thereby leading to numerical instability (Vreman *et al.* 1996, 1997).

An alternative approach for the derivation of an SGS model involves a direct employment of direct numerical simulation (DNS) data. For example, the optimal LES (Langford & Moser 1999; Völker *et al.* 2002) adopted stochastic estimation techniques (Adrian *et al.* 1989; Adrian 1990) to diminish the discrepancy between the ideal and simulated flow variables. This approach necessitated the use of multipoint correlation data as inputs, which in turn required corresponding DNS data. Moser *et al.* (2009) presented an optimal LES that did not require DNS data, but the SGS model was created based on the assumption of isotropic flow. Another example is an employment of deep learning techniques with a particular emphasis on artificial neural networks (NNs) (Sarghini *et al.* 2003; Gamahara & Hattori 2017; Maulik *et al.* 2018). Creating an SGS model through NNs requires the accumulation of extensive data through filtering DNS data. This approach is based on an assumption that there may be a complex but well-defined relationship between the SGS stress and resolved flow variables. The pioneering application of NNs in the calculation of SGS stress, to the best of our knowledge, was implemented by Sarghini *et al.* (2003). They employed an NN to find an optimal turbulent viscosity coefficient for a hybrid model (combined Smagorinsky and similarity models) applied to turbulent channel flow with nine velocity gradients and six resolved Reynolds stresses as inputs, and demonstrated its ability to accurately approximate the coefficient.

With the rapid advancement and growing recognition of deep learning (Krizhevsky *et al.* 2012; Silver *et al.* 2016), more expansive techniques have been employed to develop SGS models for diverse applications. NN-based SGS models may be classified into three categories: closed-form, reassembling, and direct NN-based SGS models, respectively. The closed-form NN-based SGS models, analogous to the study conducted by Sarghini *et al.* (2003), postulate that SGS models may be derived in a closed form from physical, empirical, or analytical tools. The coefficients of these models are adjustable, and are computed using NNs with resolved flow variables as inputs. Wollblad & Davidson (2008) identified the coefficients pertinent to proper orthogonal decomposition for turbulent channel flow through an NN. Beck *et al.* (2019) and Pawar *et al.* (2020) suggested that calculating eddy viscosity could be employed as a surrogate to the direct computation of SGS stress and contribute to enhanced stability. Moreover, Xie *et al.* (2019*a*), Xie *et al.* (2020*d*) and Wang *et al.* (2021) suggested that the SGS stress can be evaluated through a polynomial function including the strain rate, rotation rate, velocity gradient and grid size, with NNs utilized to determine the coefficients of the polynomial. Yu *et al.* (2022)

and Liu *et al.* (2023) obtained the coefficients of Smagorinsky and helicity SGS models using NN, respectively.

Reassembling NN-based SGS models extract unfiltered variables from filtered ones, and subsequently utilize these extracted variables for the computation of SGS stress. In this approach, NNs play a prominent role in the unfiltering or filtering process. Maulik *et al.* (2018) engaged NNs in the training for unfiltering (Maulik & San 2017) and filtering for two-dimensional decaying homogeneous isotropic turbulence (DHIT) in LES. The first NN collected filtered vorticity and streamfunction data across multiple grids and gauged the values of unfiltered vorticity and streamfunction at a single grid. The second NN was subsequently deployed to approximate the filtered nonlinear term, a crucial element for the determination of the SGS stress. Aligning with this methodology, Yuan *et al.* (2020) employed an NN for the estimation of SGS stresses in three-dimensional forced homogeneous isotropic turbulence (FHIT), specifically utilizing the NN to unfilter the velocities.

Direct NN-based SGS models derive the SGS stress or force directly from resolved flow variables through the application of NNs. Gamahara & Hattori (2017) employed NNs to compute the SGS stress as immediate outputs for turbulent channel flow from four input groups such as the strain rate, rotation rate, wall distance, and velocity gradient. Previous direct NN-based SGS models have used various techniques and methods to enhance model performance and stability. These include an *ad hoc* method such as wall-damping function or clipping (Gamahara & Hattori 2017; Maulik *et al.* 2019; Zhou *et al.* 2019), derivation of inputs from multiple grids for single or multiple outputs (Beck *et al.* 2019; Maulik *et al.* 2019; Xie *et al.* 2019b; Zhou *et al.* 2019; Pawar *et al.* 2020; Sirignano *et al.* 2020; Xie *et al.* 2020a,b,c; MacArt *et al.* 2021; Stoffer *et al.* 2021; Cheng *et al.* 2022; Guan *et al.* 2022; Liu *et al.* 2022; Guan *et al.* 2023), incorporation of second derivatives of velocities (Wang *et al.* 2018; Xie *et al.* 2019b; Pawar *et al.* 2020; Sirignano *et al.* 2020; Xie *et al.* 2020a; MacArt *et al.* 2021), and consideration of wall distance or filter size as inputs (Gamahara & Hattori 2017; Zhou *et al.* 2019; Abekawa *et al.* 2023). Others (Sirignano *et al.* 2020; MacArt *et al.* 2021; Guan *et al.* 2023; Sirignano & MacArt 2023) defined the training error (or objective function) using flow variables other than the SGS stresses. Sirignano *et al.* (2020), MacArt *et al.* (2021) and Sirignano & MacArt (2023) trained NNs with adjoint-based, PDE (partial differential equation)-constrained optimization methods. Other improvements involve retraining NNs through transfer learning for higher Reynolds number flows (Subel *et al.* 2021; Guan *et al.* 2022), and training NNs in complex flows (MacArt *et al.* 2021; Sirignano & MacArt 2023; Kim *et al.* 2023). On the other hand, other types of techniques to improve the performance of NN-based SGS models have also been explored, such as the utilization of convolutional neural network (Beck *et al.* 2019; Pawar *et al.* 2020; Guan *et al.* 2022; Liu *et al.* 2022; Guan *et al.* 2023), reinforcement learning (Novati *et al.* 2021; Kim *et al.* 2022; Kurz *et al.* 2023), and graph neural network (Abekawa *et al.* 2023).

Park & Choi (2021) developed a direct NN-based SGS model for turbulent channel flow whose input and output were the velocity gradient or strain rate and the SGS stress, respectively. They performed a comprehensive analysis of the salient characteristics inherent to direct NN-based SGS models, and demonstrated from a *posteriori test* without introducing *ad hoc* techniques such as wall-damping function or clipping that SGS models relying on a single grid input can compute turbulence statistics with a reasonably decent level of accuracy. In addition, two specific results from this study are noteworthy: first, when the LES grid size falls within the range of filter sizes for training NN, the SGS model successfully predicts the flow; second, the SGS model is also successful in predicting the flow at higher Reynolds number when the grid size in wall

units is same as that trained. Hence, these observations indicate that the applicability of direct NN-based SGS models depends on the dimensionless LES grid size relative to the trained grid (or filter) size. For the development of general NN-based SGS model for complex flow, it is essential that it should function properly over a wide range of non-dimensional filter or grid sizes.

Despite their promising characteristics, previous direct NN-based SGS models have confronted substantial challenges when aimed for application to untrained flows. These challenges originate from the difficulty in developing universal non-dimensional input and output variables for various flows and the nonlinear property (and thus occurrence of potentially large errors in extrapolation) of NN. To achieve regularized input and output values, various techniques have been explored, including min-max method (Xie *et al.* 2019*b*; Pawar *et al.* 2020; Wang *et al.* 2021), Gaussian normalization method (Stoffer *et al.* 2021; Cheng *et al.* 2022; Liu *et al.* 2022), normalization with root-mean-square (rms) values (Xie *et al.* 2020*c,b,a*; Guan *et al.* 2022, 2023), non-dimensionalization in wall units (Park & Choi 2021; Kim *et al.* 2022), and prescribed velocity and length scales (MacArt *et al.* 2021). However, each method has its own limitations: e.g., it requires an equilibrium state or homogeneous direction(s), does not show generalizability when switched to other flows, or proves to be infeasible as it requires DNS results. Consequently, a plausible approach toward general direct NN-based SGS models would be to employ only local variables for non-dimensionalization, like those described in Prakash *et al.* (2022) and Abekawa *et al.* (2023). On the other hand, two strategies may be proposed for the issue of extrapolation errors of NN. The first strategy is to discover normalized flow variables and SGS stresses that are bounded within a certain range for various flows. The second strategy is to incorporate all accessible data to cover an exhaustive range of flow fields. The former presents considerable challenges, because it requires a formidable task of pinpointing normalized flow variables that remain invariant with respect to factors like the Reynolds number, filter size, and flow topology. The latter may demand DNS data of various flows at fairly high Reynolds numbers and thus imposes a huge computational burden.

Therefore, the objective of the present study is to devise a new NN-based SGS model designed to overcome the limitations of existing direct NN-based SGS models. We modify the structure of an NN and formulate a recursive process to generate an SGS model valid for a wide range of grid sizes. Here, an NN is trained using fDNS data at low Reynolds number and then updated by data at higher Reynolds number collected through filtered LES. To validate the performance of the present recursive NN-based SGS model, several SGS models are employed to simulate FHIT at various Reynolds numbers. In addition, two DHIT cases are simulated using the NN trained with FHIT. Section 2 provides the LES framework, NN-based SGS models under consideration, FHIT and filtering method employed. Section 3 describes the recursive algorithm for constructing recursive NN-based SGS models, and provides the results of *a priori* and *a posteriori* tests. In section 4, the present SGS models are applied to FHIT at high Reynolds numbers and DHIT, respectively, and the results are discussed, followed by conclusions in section 5.

2. Numerical details

2.1. Large eddy simulation

In LES, the flow variables are filtered using the following operation:

$$\bar{\phi}(\mathbf{x}, t) = \int \bar{G}(\mathbf{r}, \mathbf{x}) \phi(\mathbf{x} - \mathbf{r}, t) d\mathbf{r}, \quad (2.1)$$

$$\int \bar{G}(\mathbf{r}, \mathbf{x}) d\mathbf{r} = 1, \quad (2.2)$$

where $\bar{\phi}$ is a filtered flow variable, \bar{G} is a filter function, \mathbf{x} and \mathbf{r} denote position vectors, and t is time. The spatially filtered continuity and Navier-Stokes equations for incompressible flows are

$$\frac{\partial \bar{u}_i}{\partial x_i} = 0, \quad (2.3)$$

$$\frac{\partial \bar{u}_i}{\partial t} + \frac{\partial \bar{u}_i \bar{u}_j}{\partial x_j} = -\frac{1}{\rho} \frac{\partial \bar{p}^*}{\partial x_i} + \nu \frac{\partial^2 \bar{u}_i}{\partial x_j \partial x_j} - \frac{\partial \tau_{ij}^r}{\partial x_j}, \quad (2.4)$$

where x_i 's are the coordinates (x, y, z) , u_i 's are the corresponding velocities (u, v, w) , and ρ and ν are the fluid density and kinetic viscosity, respectively. The effect of the SGS eddy motions is modeled as anisotropic part of SGS stress, τ_{ij}^r :

$$\tau_{ij} = \overline{u_i u_j} - \bar{u}_i \bar{u}_j, \quad (2.5)$$

$$\tau_{ij}^r = \tau_{ij} - \frac{1}{3} \tau_{kk} \delta_{ij}, \quad (2.6)$$

where δ_{ij} is the Kronecker delta. The filtered pressure \bar{p}^* includes the isotropic components of SGS stress:

$$\bar{p}^* = \bar{p} + \frac{1}{3} \rho \tau_{kk}. \quad (2.7)$$

In case of HIT, the filtered continuity and Navier-Stokes equations can be transformed in a spectral space. The pseudo-spectral method is utilized for spatial discretization, and the zero-padding method, augmented with the 3/2 rule, is applied to control aliasing errors. For temporal integration, a third-order Runge-Kutta method is used for the convection term, and the second-order Crank-Nicolson method is applied to the diffusion term.

To evaluate the performance of an NN-based SGS model relative to those of traditional SGS models, LESs with the constant Smagorinsky model (CSM, Smagorinsky (1963)), dynamic Smagorinsky model (DSM, Germano *et al.* (1991); Lilly (1992)), and gradient model (GM, Clark *et al.* (1979)) are carried out. The Smagorinsky models determine the anisotropic component of SGS stress from

$$\tau_{ij}^r = -2(C_s \bar{\Delta})^2 |\bar{S}| \bar{S}_{ij}, \quad (2.8)$$

where C_s is the Smagorinsky model coefficient, $\bar{\Delta}$ is the grid size, $\bar{S}_{ij} = (1/2)(\partial \bar{u}_i / \partial x_j + \partial \bar{u}_j / \partial x_i)$, and $|\bar{S}| = \sqrt{2 \bar{S}_{ij} \bar{S}_{ij}}$. For CSM, C_s is a fixed value of 0.17. For DSM, the Smagorinsky model coefficient is obtained as

$$(C_s \bar{\Delta})^2 = \max \left[-\frac{1}{2} \langle L_{ij} M_{ij} \rangle_h / \langle M_{ij} M_{ij} \rangle_h, 0 \right], \quad (2.9)$$

where

$$L_{ij} = \widetilde{\bar{u}_i \bar{u}_j} - \widetilde{\bar{u}_i} \widetilde{\bar{u}_j}, \quad (2.10)$$

$$M_{ij} = \left(\frac{\widetilde{\bar{\Delta}}}{\bar{\Delta}} \right)^2 |\widetilde{\bar{S}}| \widetilde{\bar{S}}_{ij} - \widetilde{|\bar{S}| \bar{S}_{ij}}, \quad (2.11)$$

$\widetilde{(\cdot)}$ and $\widetilde{\widetilde{(\cdot)}}$ correspond to the grid- and test-filtering operations, respectively, and $\widetilde{\bar{\Delta}} = 2\bar{\Delta}$. The notation $\langle \cdot \rangle_h$ denotes an instantaneous averaging over homogeneous directions. The SGS stress in GM is derived through the application of Taylor expansions of the filtered

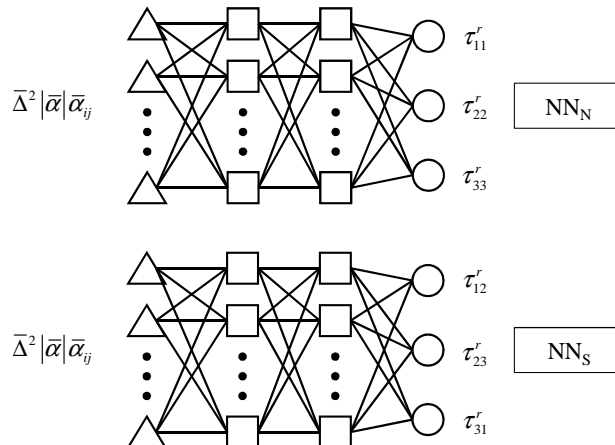


FIGURE 1. Schematic diagram of the present NN-based SGS model that consists of a dual NN: NN_N and NN_S predict the SGS normal and shear stresses, respectively.

velocity (Clark *et al.* 1979; Vreman *et al.* 1996) as

$$\tau_{ij} = \frac{1}{12} \sum_k \bar{\Delta}_k^2 \frac{\partial \bar{u}_i}{\partial x_k} \frac{\partial \bar{u}_j}{\partial x_k}, \quad (2.12)$$

and τ_{ij}^r is computed from (2.6), where $\bar{\Delta}_k$ is the grid size in x_k direction.

2.2. NN-based SGS model

So far, most NN-based SGS models have optimized the weights and biases of the NNs, despite utilizing different deep learning techniques (see §1). For example, Park & Choi (2021) implemented an NN consisting of two hidden layers and 128 neurons per hidden layer to compute six components of the SGS stress:

$$\left. \begin{aligned} h_i^{(1)} &= \bar{q}_i & (i = 1, 2, \dots, N_q); \\ h_j^{(2)} &= \max \left[0, \gamma_j^{(2)} \left(\sum_{i=1}^{N_q} W_{ij}^{(1)(2)} h_i^{(1)} + b_j^{(2)} - \mu_j^{(2)} \right) / \sigma_j^{(2)} + \beta_j^{(2)} \right] & (j = 1, 2, \dots, 128); \\ h_k^{(3)} &= \max \left[0, \gamma_k^{(3)} \left(\sum_{j=1}^{128} W_{jk}^{(2)(3)} h_j^{(2)} + b_k^{(3)} - \mu_k^{(3)} \right) / \sigma_k^{(3)} + \beta_k^{(3)} \right] & (k = 1, 2, \dots, 128); \\ h_l^{(4)} &= s_l = \sum_{k=1}^{128} W_{kl}^{(3)(4)} h_k^{(3)} + b_l^{(4)} & (l = 1, 2, \dots, 6). \end{aligned} \right\} \quad (2.13)$$

Here, \bar{q} is the grid-filtered input, N_q is the number of the input components, $\mathbf{W}^{(m)(m+1)}$ is the weight matrix between m th and $(m+1)$ th layers, $\mathbf{b}^{(m)}$ is the bias vector of the m th layer, \mathbf{s} is the output (six components of the SGS stress), and $\gamma^{(m)}$, $\mu^{(m)}$, $\sigma^{(m)}$ and $\beta^{(m)}$ are the parameters for batch normalization (Ioffe & Szegedy 2015). During an NN training process, the parameters $\mathbf{W}^{(m)(m+1)}$ and $\mathbf{b}^{(m+1)}$ are optimized to minimize the training error.

In the present study, we construct an NN-based SGS model using a dual NN architecture (figure 1), where the output of one NN (NN_N) is the SGS normal stresses

$(\tau_{11}^r, \tau_{22}^r, \tau_{33}^r)$, and that of the other (NN_S) is the SGS shear stresses $(\tau_{12}^r, \tau_{13}^r, \tau_{23}^r)$. The reason of using two NNs is that the ranges of the normal and shear SGS stresses are quite different from each other and thus separate treatments of these SGS stresses increase the prediction capability of the present NN-based SGS model. Each of the present NNs consists of two hidden layers and 64 neurons per hidden layer, and the output of the m -th layer, $\mathbf{h}^{(m)}$, is computed as

$$\left. \begin{aligned} h_i^{(1)} &= \bar{q}_i & (i = 1, 2, \dots, 9); \\ h_j^{(2)} &= \max \left[0.02r_j^{(2)}, r_j^{(2)} \right], \quad r_j^{(2)} = \sum_{i=1}^9 W_{ij}^{(1)(2)} h_i^{(1)} & (j = 1, 2, \dots, 64); \\ h_k^{(3)} &= \max \left[0.02r_k^{(3)}, r_k^{(3)} \right], \quad r_k^{(3)} = \sum_{j=1}^{64} W_{jk}^{(2)(3)} h_j^{(2)} & (k = 1, 2, \dots, 64); \\ h_l^{(4)} &= s_l = \sum_{k=1}^{64} W_{kl}^{(3)(4)} h_k^{(3)} & (l = 1, 2, 3). \end{aligned} \right\} \quad (2.14)$$

Note that we remove the bias \mathbf{b} and parameters for batch normalization ($\boldsymbol{\gamma}$, $\boldsymbol{\mu}$, $\boldsymbol{\sigma}$ and $\boldsymbol{\beta}$). Also, we use the leaky rectified linear unit function (leaky ReLU) as an activation function: $f(x) = \max[ax, x]$, which was proposed by Maas *et al.* (2013) to overcome vanishing gradient problem (Bengio *et al.* 1994). The negative slope is determined to be $0.01 \leq a \leq 0.2$ (Xu *et al.* 2015), and we choose $a = 0.02$. Without the bias and batch-normalization parameters and with the use of leaky ReLU, the present NN complies with the following conditions:

$$\mathbf{NN}(c\mathbf{A}) = c\mathbf{NN}(\mathbf{A}) \quad \text{only if } c \geq 0, \quad (2.15)$$

$$\mathbf{NN}(\mathbf{A} + \mathbf{B}) \neq \mathbf{NN}(\mathbf{A}) + \mathbf{NN}(\mathbf{B}), \quad (2.16)$$

where c is a positive scalar, and \mathbf{A} and \mathbf{B} are arbitrary tensors. Thus, the present NN still retains its nonlinearity, making it suitable for nonlinear regression between the SGS stresses and local flow variables. Equation (2.15) allows us to apply an NN trained from one flow to another flow (see §3.2).

During the training process, the weight parameters $\mathbf{W}^{(m)(m+1)}$ are optimized to minimize the mean square error given by

$$L = \frac{1}{3} \frac{1}{N_b} \sum_{l=1}^3 \sum_{n=1}^{N_b} (s_{l,n}^{\text{fDNS}} - s_{l,n})^2, \quad (2.17)$$

where N_b denotes the minibatch size of 256, and $s_{l,n}^{\text{fDNS}}$ corresponds to the anisotropic components τ_{ij}^r obtained from fDNS.

We apply Adam algorithm (a type of gradient descent, Kingma & Ba (2014)) and learning rate annealing method (Simonyan & Zisserman 2014; He *et al.* 2016) to optimize the weights and enhance the training speed, respectively. Early stopping (Goodfellow *et al.* 2016) is employed in the training process to avoid overfitting. The learning rate is initially 0.025, and is subsequently reduced by a factor of 10 if no improvement in the training error is observed over five epochs. If the learning rate is decreased three times but there is no reduction in the training error over five epochs, training is stopped. The entire process to train and execute the present NN is carried out with the PyTorch open-source library in the Python programming environment.

We develop an NN-based SGS model (velocity gradient model, called VGM hereafter) whose input and output are $\bar{\Delta}^2 |\bar{\alpha}| \bar{\alpha}_{ij}$ and τ_{ij}^r , respectively, where $\bar{\Delta} = (\bar{\Delta}_x \bar{\Delta}_y \bar{\Delta}_z)^{1/3}$,

Case	N_{DNS}	Re_L	Re_λ
DNS128	128	149.09	93.03
DNS256	256	375.69	154.17
DNS512	512	946.67	-
DNS1024	1024	2385.46	-
DNS2048	2048	6010.98	-
DNS4096	4096	15146.71	-
DNS8192	8192	38167.31	-
DNS16384	16384	96175.60	-
DNS32768	32768	242347.33	-

TABLE 1. Cases of DNS at various Reynolds numbers for FHIT. Here, $Re_L = (N_{\text{DNS}}/3)^{4/3}$ and $\Delta_{\text{DNS}}/\eta = 2\pi/3$ ($N_{\text{DNS}}\Delta_{\text{DNS}} = 2\pi L$). DNSs are performed for DNS128 and DNS256, and the corresponding Re_λ 's are given in this table.

$\bar{\alpha}_{ij} = \partial \bar{u}_i / \partial x_j$, and $|\bar{\alpha}| = \sqrt{\bar{\alpha}_{ij}\bar{\alpha}_{ij}}$. Note that the dimensions of input and output are matched to be the same. The velocity gradient tensor as an input has been used by many previous studies (Gamahara & Hattori 2017; Wang *et al.* 2018; Zhou *et al.* 2019; Xie *et al.* 2019b; Pawar *et al.* 2020; Prat *et al.* 2020; Xie *et al.* 2020c,b,a; Park & Choi 2021; Kim *et al.* 2022; Abekawa *et al.* 2023), and the same form of input was considered by Jamaat & Hattori (2022) for one-dimensional Burgers turbulence. The VGM obtains inputs from each grid point and compute corresponding SGS stresses.

2.3. Forced homogeneous isotropic turbulence (FHIT) and filtering method

FHIT involves an additional forcing term in the Navier-Stokes equations at low wavenumbers (Ghosal *et al.* 1995; Rosales & Meneveau 2005; Park *et al.* 2006):

$$f_i = \epsilon_t \frac{u_i}{\sum_{0 < |\mathbf{k}| < 2} |\hat{u}_i(\mathbf{k})|^2}, \quad (2.18)$$

where f_i is the forcing term, \hat{u}_i is the Fourier coefficient of u_i , ϵ_t is the prescribed mean total dissipation rate determining the turbulent energy injection rate, $|\mathbf{k}| = \sqrt{k_x^2 + k_y^2 + k_z^2}$, and k_i is the wavenumber in i direction. Note that ϵ_t encompasses both the resolved and modeled dissipation.

In FHIT, two distinct Reynolds numbers, $Re_\lambda = u_{\text{rms}}\lambda/\nu$ and $Re_L = UL/\nu$, can be defined. Here, u_{rms} is the rms velocity fluctuations, $\lambda (= \sqrt{15}u_{\text{rms}}^2\nu/\epsilon_t)$ is the Taylor microscale, L is associated with the computational domain size of $2\pi L \times 2\pi L \times 2\pi L$, and ϵ_t is normalized to unity such that $\epsilon_t L/U^3 = 1$. The Taylor microscale Reynolds number Re_λ has been widely used in turbulence studies. Nevertheless, the extraction of u_{rms} requires intricate experimental data or DNS. In contrast, Re_L does not require such preliminary outcomes, and can be deduced from $\epsilon_t L/U^3 = 1$, $\eta k_{\text{max,DNS}}$ and N_{DNS} , where η is the Kolmogorov length scale, and $k_{\text{max,DNS}}$ and N_{DNS} are the largest wavenumber and number of grid points in each direction in DNS, respectively. According to Pope (2000), $\eta k_{\text{max,DNS}} = 3/2$ or $\Delta_{\text{DNS}}/\eta = 2\pi/3$ is set to achieve sufficiently high resolution in DNS, where Δ_{DNS} is the grid size in DNS. Then, $L = \Delta_{\text{DNS}}N_{\text{DNS}}/(2\pi) = \eta N_{\text{DNS}}/3$. With these relations together with $\eta = (\nu^3/\epsilon_t)^{1/4}$, one can obtain $Re_L = (N_{\text{DNS}}/3)^{4/3}$. Table 1 lists the cases of DNS at various Reynolds numbers by changing the number of grid points for FHIT, where each case is named as $\text{DNS}N_{\text{DNS}}$. Note that the cases listed in table 1 do not necessarily require actual DNS except for the case of DNS128 (the recursive

Case	N_c	Re_L	$\bar{\Delta}/\eta$
fDNS32/128 or LES32/128	32	149.09	8.38
fDNS64/128	64	149.09	4.19
fDNS32/256 or LES32/256	32	375.69	16.76
fDNS64/256 or LES64/256	64	375.69	8.38
fDNS128/256	128	375.69	4.19
LES64/512	64	946.67	16.76
LES64/1024	64	2385.46	33.51

TABLE 2. Cases of fDNS and LES at various Reynolds numbers for FHIT. Here, N_c is the number of grid points in each direction for fDNS or LES, and $\bar{\Delta}$ denotes the filter size for fDNS ($\bar{\Delta}_{\text{fDNS}}$) or the grid size for LES ($\bar{\Delta}_{\text{LES}}$). The name of each case indicates fDNS N_c/N_{DNS} or LES N_c/N_{DNS} . Note that $\Delta_{\text{DNS}}/\eta = 2\pi/3$.

Filter	$\hat{G}(\mathbf{k})$	Largest wavenumber of filtered variables
Spectral cut-off	$H(k_c - k)$	k_c
Gaussian	$\exp(-k^2 \bar{\Delta}^2/24)$	$k_{\text{DNS}} (= \pi/\Delta_{\text{DNS}})$
Cut-Gaussian	$\exp(-k^2 \bar{\Delta}^2/24)$	k_c

TABLE 3. Comparison of three filters. Here, H is the Heaviside step function.

procedure introduced in the below requires DNS only at a low Reynolds number), and LESs are conducted for higher Reynolds number cases through the recursive procedure.

Table 2 shows the cases considered for fDNS and LES of FHIT. The fDNS data are obtained by applying a transfer function $\hat{G}(\mathbf{k})$ to the Fourier-transformed DNS data $\hat{u}_i(\mathbf{k})$:

$$\hat{u}_i(\mathbf{k}) = \hat{u}_i(\mathbf{k}) \hat{G}(\mathbf{k}), \quad (2.19)$$

$$\hat{G}(\mathbf{k}) = \int \exp(i\mathbf{k} \cdot \mathbf{r}) \bar{G}(\mathbf{r}) d\mathbf{r}. \quad (2.20)$$

The fDNS data can be obtained by applying a spectral cut-off filter or Gaussian filter in the spectral space. However, these filterings have limitations when the filtered variables are compared with LES results. The spectral cut-off filtering removes the Fourier coefficients \hat{u}_i at $k > k_c$, and allows filtered variables to be placed on coarser grids of LES, where $k_c (= \pi/\bar{\Delta})$ is the cut-off wavenumber. However, this filtering fails to satisfy the realizability condition due to negative weights in the physical space (Vreman. *et al.* 1994). Additionally, the spectral cut-off filtering may exhibit non-local oscillations (Meneveau & Katz 2000; Pope 2000). On the other hand, the Gaussian filtering is free from these drawbacks, and requires filtering even when the wavenumber exceeds the LES limit (i.e., $k > \pi/\bar{\Delta}_{\text{LES}}$). Although the filter size may coincide with the LES grid size, the Gaussian filtered data are allocated at DNS grids, not at LES grids.

In the present study, we use the cut-Gaussian filtering (Zanna & Bolton 2020; Guan *et al.* 2022, 2023; Pawar *et al.* 2023) which retains the transfer function of Gaussian filtering but truncates the filtered variables at the wavenumbers exceeding the cut-off wavenumber k_c . Table 3 shows three different filters in the spectral space, corresponding transfer functions, and largest wavenumbers of filtered variables, respectively. Figure 2 shows the energy spectra from DNS128, fDNS32/128's using cut-Gaussian, Gaussian and spectral cut-off filters, and LES32/128's with DSM and GM, respectively. The energy

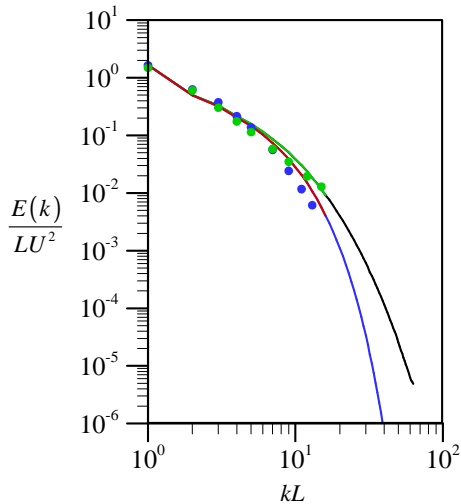


FIGURE 2. Three-dimensional energy spectra: —, DNS128 ($Re_L = 149.09$; $Re_\lambda = 93.03$); —, fDNS32/128 with cut-Gaussian filtering; —, fDNS32/128 with Gaussian filtering; —, fDNS32/128 with spectral cut-off filtering; •, LES32/128 with DSM; •, LES32/128 with GM.

spectrum with GM is in an excellent agreement with that of fDNS using the spectral cutoff filter. In contrast, the energy spectrum with DSM is closer to that of fDNS using the cut-Gaussian filter. Given the increased adaptability of DSM over GM, we measure the prediction capability of the SGS models based on the cut-Gaussian filtered DNS data.

3. A recursive NN-based SGS model

3.1. A recursive algorithm

The present study employs a recursive method to construct an NN-based SGS model adapted to various grid sizes normalized by the Kolmogorov length scale from the following steps:

- (i) Obtain training data (fDNS data) by filtering DNS data at a low Reynolds number (Re_L);
- (ii) Train an NN-based SGS model with the fDNS data;
- (iii) Apply the NN-based SGS model to LES at a higher Reynolds number, where the ratio of LES grid size to the Kolmogorov length scale ($\bar{\Delta}_{LES}/\eta$) is equal to that of filter size to the Kolmogorov length scale ($\bar{\Delta}_{fDNS}/\eta$);
- (iv) Filter the LES data and include the filtered LES (fLES) data in the training dataset, where the new filter size is twice the LES grid size;
- (v) Train the NN-based SGS model using the augmented training data;
- (vi) Apply the updated NN-based SGS model to LES at even higher Reynolds number, where the LES grid size is equal to the filter size defined in step (iv);
- (vii) Repeat from step (iv) to (vi) for LES at higher Reynolds numbers.

The steps (i) and (ii) are similar to those used in constructing previous NN-based SGS models. The present recursive method aims at improving the performance of an NN-based

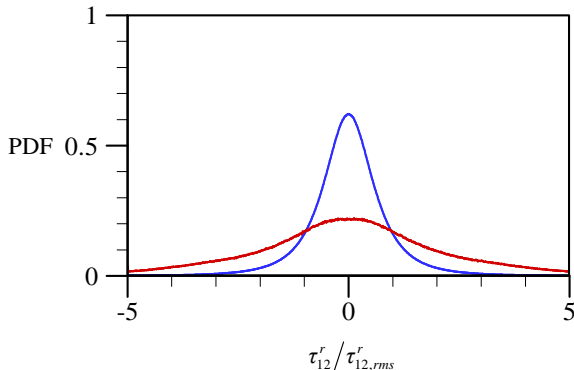


FIGURE 3. Probability density function (PDF) of normalized τ_{12}^r before (—) and after (—) undersampling.

SGS model at a wider range of non-dimensional grid sizes by recursively performing LES and training it using fLES data.

3.2. NN-based SGS model trained with fDNS data: a priori and a posteriori tests

First, fDNS data is used to train an NN. The Reynolds number and number of grid points in each direction are $Re_L = 149.09$ and $N_{\text{DNS}} = 128$, respectively (table 1). The filter sizes considered are $\bar{\Delta}_{\text{fDNS}}/\eta = 8.38$ and 4.19 , corresponding to the cases of fDNS32/128 and fDNS64/128, respectively (table 2). Including two different filter sizes in constructing fDNS data helps to improve the prediction capability of NN-based SGS models (see, for example, Park & Choi (2021)) by broadening the ranges of the input and output, when they are appropriately normalized. In the present study, we train a dual NN (NN_N and NN_S in figure 1) with the training data (input and output) normalized by rms SGS normal ($\tau_{11,rms}^r$) and shear ($\tau_{12,rms}^r$) stress fluctuations, respectively. Note that $\tau_{11,rms}^r (= \tau_{22,rms}^r = \tau_{33,rms}^r)$ and $\tau_{12,rms}^r (= \tau_{13,rms}^r = \tau_{23,rms}^r)$ are obtained from (2.5) and (2.6) with DNS data. During actual LES, however, the SGS normal and shear stress fluctuations are *a priori* unknown, and thus providing normalized input data to the NN is not possible. Hence, in actual LES, we can only provide the input normalized by the characteristic velocity scale ($\bar{\Delta}^2 |\bar{\alpha}| \bar{\alpha}_{ij} / U_{\text{LES}}^2$). Thanks to the important property of the present NN, (2.15), we obtain the following relation: (no summation on i and j)

$$\frac{\tau_{ij}^r}{U_{\text{LES}}^2} = \frac{\tau_{ij,rms}^r}{U_{\text{LES}}^2} \frac{\tau_{ij}^r}{\tau_{ij,rms}^r} = \frac{\tau_{ij,rms}^r}{U_{\text{LES}}^2} \text{NN} \left(\frac{\bar{\Delta}^2 |\bar{\alpha}| \bar{\alpha}_{ij}}{\tau_{ij,rms}^r} \right) = \text{NN} \left(\frac{\bar{\Delta}^2 |\bar{\alpha}| \bar{\alpha}_{ij}}{U_{\text{LES}}^2} \right). \quad (3.1)$$

This relation indicates that, during actual LES, one can provide the input normalized by U_{LES} to the NN trained with the input normalized by the rms SGS stresses.

On the other hand, the SGS stresses obtained from DNS data have a problem of imbalanced distribution because they tend to be mainly distributed around zero. So, we choose the normalized output and corresponding input through the process known as undersampling (Drummond & Holte 2003; Liu *et al.* 2008). During this process, we do not use all the filtered data as training one, but choose data such that the possibility of choosing data as training one decreases when its magnitude is near to zero: i.e., the probability (\mathcal{P}) to choose an SGS shear stress and corresponding inputs as training data

Re_L	SGS model	$R(\tau_{11}^r)$	$R(\tau_{12}^r)$	$R(\epsilon_{SGS})$	ϵ_{SGS}
149.09	fDNS32/128	—	—	—	0.430
	VGM(32+64)/128	0.661	0.692	0.647	0.439
	CSM32/128	0.191	0.204	0.569	1.077
	DSM32/128	0.191	0.204	0.569	0.859
	GM32/128	0.653	0.682	0.633	0.315
375.69	fDNS64/256	—	—	—	0.439
	VGM(32+64)/128	0.664	0.695	0.662	0.453
	VGM(64+128)/256	0.664	0.695	0.662	0.449
	CSM64/256	0.186	0.201	0.578	1.118
	DSM64/256	0.186	0.201	0.577	0.892
	GM64/256	0.656	0.686	0.647	0.324

TABLE 4. Statistics from *a priori* tests at $Re_L = 149.09$ and 375.69 with $\bar{\Delta}_{\text{fDNS}}/\eta = 8.38$: Pearson correlation coefficients (R) of τ_{ij}^r and SGS dissipation $\epsilon_{SGS} (= -\tau_{ij}^r \bar{S}_{ij})$, and magnitude of ϵ_{SGS} .

is

$$\left. \begin{aligned} \mathcal{P} &= \sin^2 \theta & \text{if } \theta < \frac{\pi}{2} \\ \mathcal{P} &= 1 & \text{if } \theta \geq \frac{\pi}{2} \end{aligned} \right\}, \quad (3.2)$$

$$\theta = \frac{\pi}{8} \sqrt{\frac{\{(\tau_{12}^r)^2 + (\tau_{23}^r)^2 + (\tau_{13}^r)^2\}/3}{\tau_{12,rms}^r}}.$$

Figure 3 illustrates the effect of undersampling on the distribution of training data. This undersampling reduces the probability of zero SGS stresses, and enhances the occurrence of strong SGS stresses, leading to generate high SGS dissipation and thus improving the performance of an NN-based SGS model. The SGS normal stresses are also similarly processed. For each fDNS dataset, about 500,000 pairs of $\bar{\Delta}^2 |\bar{\alpha}| \bar{\alpha}_{ij}$ and τ_{ij}^r are used for training.

We perform *a priori* tests with the present VGMs and traditional models using fDNS32/128 ($Re_L = 149.09$) and fDNS64/256 ($Re_L = 375.69$), respectively. Table 4 provides the correlations of the SGS normal and shear stresses and SGS dissipation, and the magnitude of the SGS dissipation from various SGS models, respectively. Here, VGM(32+64)/128 is trained using fDNS32/128 and fDNS64/128 datasets, and VGM(64+128)/256 is done using fDNS64/256 and fDNS128/256 datasets, respectively. For both Reynolds numbers, VGMs provide the highest correlations of the SGS stresses and the magnitudes of the SGS dissipation closest to those of fDNS data. It is notable to see that VGM(32+64)/128 trained at $Re_L = 149.09$ successfully predicts the correlations and SGS dissipation even when it is applied to a higher Reynolds number of $Re_L = 375.69$.

Figures 4(a) and (b) show the PDFs of ϵ_{SGS} , τ_{11}^r and τ_{12}^r from various SGS models for $Re_L = 149.09$ and 375.69 , respectively. As shown, the PDFs of ϵ_{SGS} from VGM and GM agree very well with fDNS data. The PDFs from both CSM and DSM appear only at positive SGS dissipation but do not agree well with fDNS data. Similarly, for SGS stresses, VGM and GM work very well, whereas CSM and DSM are not good. It should be noted that VGM(32+64)/128 trained at $Re_L = 149.09$ predicts the PDFs accurately at $Re_L = 375.69$ as much as VGM(64+128)/256 does.

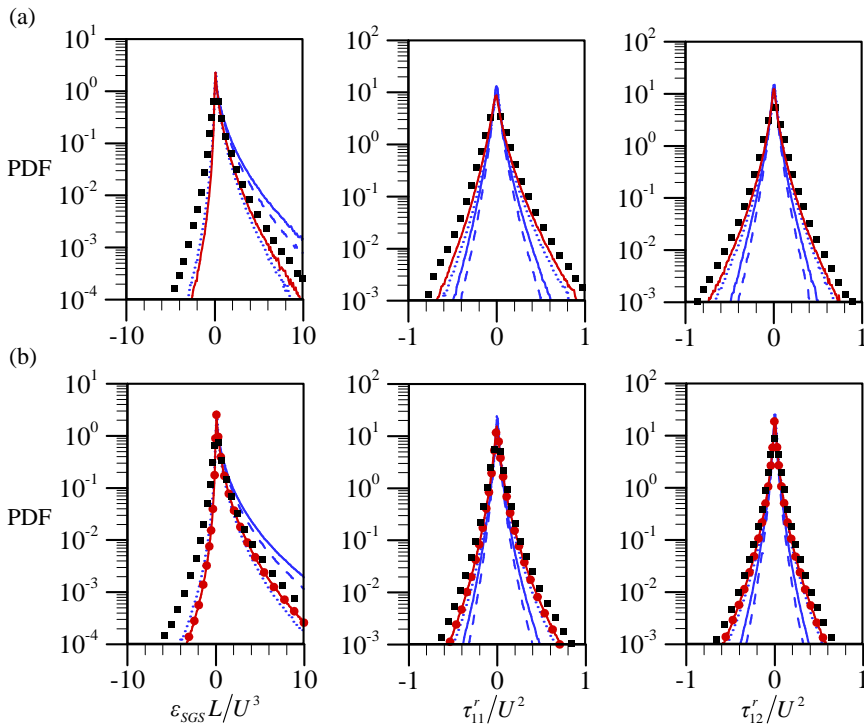


FIGURE 4. Probability density functions of the SGS dissipation and SGS normal and shear stresses (*a priori* test with $\Delta_{\text{fDNS}}/\eta = 8.38$): (a) $Re_L = 149.09$; (b) $Re_L = 375.69$. In (a), \blacksquare , fDNS32/128; --- , VGM(32+64)/128; --- , CSM32/128; - - - , DSM32/128; , GM32/128. In (b), \blacksquare , fDNS64/256; \bullet , VGM(64+128)/256; --- , VGM(32+64)/128; --- , CSM64/256; - - - , DSM64/256; , GM64/256.

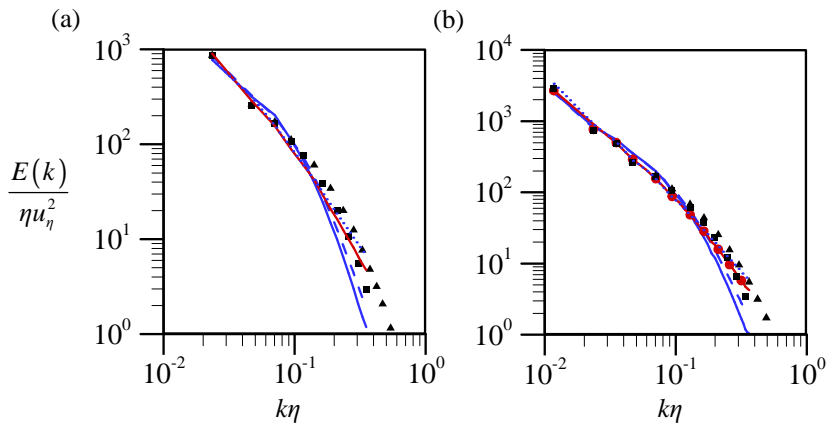


FIGURE 5. Three-dimensional energy spectra (*a posteriori* test; LES32/128 and LES64/256 for $Re_L = 149.09$ and 375.69 , respectively, with $\Delta_{\text{LES}}/\eta = 8.38$): (a) $Re_L = 149.09$; (b) $Re_L = 375.69$. In (a), \blacktriangle , DNS128; \blacksquare , fDNS32/128; --- , VGM(32+64)/128; --- , CSM32/128; - - - , DSM32/128; , GM32/128. In (b), \blacktriangle , DNS256; \blacksquare , fDNS64/256; \bullet , VGM(64+128)/256; --- , VGM(32+64)/128; --- , CSM64/256; - - - , DSM64/256; , GM64/256. Here, u_η is the Kolmogorov velocity scale.

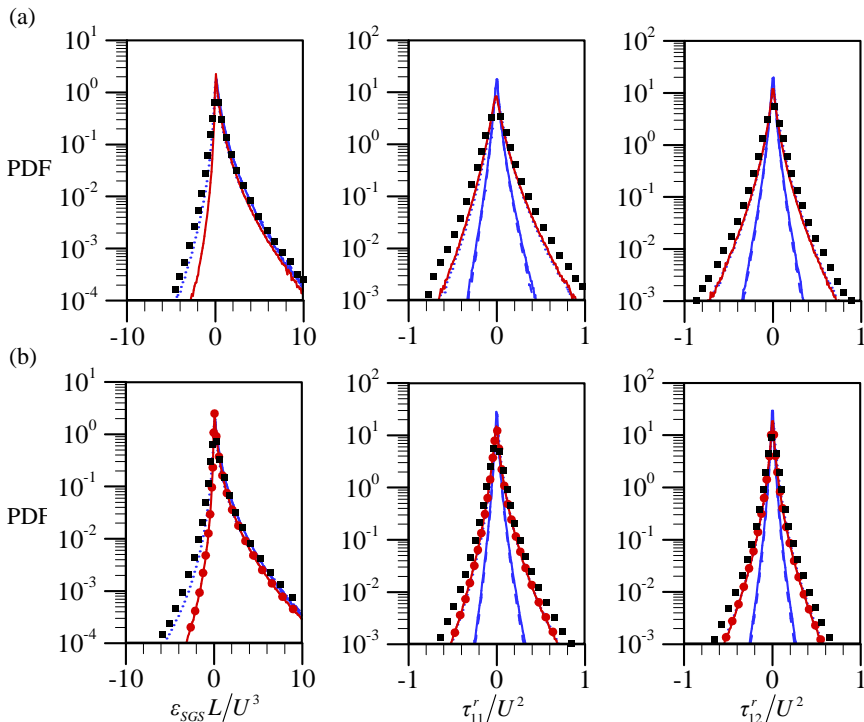


FIGURE 6. Probability density functions (*a posteriori* test; LES32/128 and LES64/256 for $Re_L = 149.09$ and 375.69 , respectively, with $\bar{\Delta}_{LES}/\eta = 8.38$): (a) $Re_L = 149.09$; (b) $Re_L = 375.69$. In (a), \blacksquare , fDNS32/128; --- , VGM(32+64)/128; --- , CSM32/128; --- , DSM32/128; \cdots , GM32/128. In (b), \blacksquare , fDNS64/256; \bullet , VGM(64+128)/256; --- , VGM(32+64)/128; --- , CSM64/256; --- , DSM64/256; \cdots , GM64/256.

Now, we perform *a posteriori* tests (actual LES) with the present VGMs and traditional models for $Re_L = 149.09$ and 375.69 , and compare the results with fDNS32/128 and fDNS64/256 data, respectively. Figures 5 and 6 show the three-dimensional energy spectra and PDFs of the SGS dissipation and SGS stresses, respectively. The energy spectra from VGM and GM agree well with fDNS data and better than those of CSM and DSM. For PDFs, GM provides the most accurate predictions and VGM also performs very well, whereas those from CSM and DSM are not good. These results indicate that LES with VGM trained at a Reynolds number predicts turbulence statistics very well for a different (higher) Reynolds number flow if $\bar{\Delta}_{LES}/\eta = \bar{\Delta}_{fDNS}/\eta$. A similar conclusion was also made by Park & Choi (2021), where the grid size was non-dimensionalized in wall units rather than by the Kolmogorov length scale.

3.3. NN-based SGS model trained with fDNS and fLES data: *a priori* and *a posteriori* tests

As mentioned before, we train the NN with fLES data as well as fDNS data. The theoretical basis for filtering LES data can be attributed to the test filter introduced by Germano *et al.* (1991):

$$\tilde{\phi}(\mathbf{x}, t) = \int \tilde{G}(\mathbf{r}, \mathbf{x}) \phi(\mathbf{x} - \mathbf{r}, t) d\mathbf{r}, \quad (3.3)$$

SGS model	Training data
VGM128D	fDNS32/128, fDNS64/128
VGM256DD	fDNS64/256, fDNS128/256
VGM(128D+256D)	fDNS32/128, fDNS64/128, fDNS32/256
VGM(128D+256L)	fDNS32/128, fDNS64/128, fLES32/256
VGM(128D+1024L)	fDNS32/128, fDNS64/128, fLES32/256, fLES32/512, fLES32/1024
VGM(128D+32768L)	fDNS32/128, fDNS64/128, fLES32/256, fLES32/512, fLES32/1024, fLES32/2048, fLES32/4096, fLES32/8192, fLES32/16384, fLES32/32768

TABLE 5. VGMs and corresponding training data. Here, VGM128D and VGM256DD are the same as VGM(32+64)/128 and VGM(64+128)/256 discussed in §3.2, respectively.

SGS model	$R(\tau_{11}^r)$	$R(\tau_{12}^r)$	$R(\epsilon_{SGS})$	ϵ_{SGS}
fDNS32/256	—	—	—	0.734
VGM(128D+256D)	0.528	0.563	0.540	0.653
VGM(128D+256L)	0.527	0.563	0.539	0.706
CSM32/256	0.196	0.221	0.489	1.397
DSM32/256	0.196	0.221	0.489	1.316
GM32/256	0.511	0.544	0.507	0.378

TABLE 6. Statistics from *a priori* test at $Re_L = 375.69$ with $\bar{\Delta}/\eta = 16.76$: Pearson correlation coefficients (R) of τ_{ij}^r and ϵ_{SGS} , and magnitude of ϵ_{SGS} .

where \tilde{G} is a filter function and $\tilde{\tilde{G}} = \tilde{G}\tilde{G}$. The test-filtered SGS stresses are written as

$$T_{ij} = \widetilde{\widetilde{u_i u_j}} - \widetilde{\widetilde{u_i}} \widetilde{\widetilde{u_j}}, \quad (3.4)$$

$$T_{ij}^r = T_{ij} - \frac{1}{3} T_{kk} \delta_{ij}, \quad (3.5)$$

and T_{ij}^r is obtained by the following relations:

$$T_{ij}^r = \widetilde{\widetilde{\tau_{ij}^r}} + L_{ij}^r, \quad (3.6)$$

where

$$L_{ij} = \widetilde{\widetilde{u_i u_j}} - \widetilde{\widetilde{u_i}} \widetilde{\widetilde{u_j}}, \quad (3.7)$$

$$L_{ij}^r = L_{ij} - \frac{1}{3} L_{kk} \delta_{ij}. \quad (3.8)$$

The present VGM is updated through the accumulation of new datasets with the input of $\tilde{\Delta}^2 |\tilde{\alpha}| \tilde{\alpha}_{ij}$ and the output of T_{ij}^r . The test filter size is twice the LES grid size, i.e., $\tilde{\Delta} = 2\tilde{\Delta}_{LES}$. The filtered LES data, referred to as fLES32/256, are obtained by filtering LES64/256 data. The fLES data is selected using the same normalization and undersampling techniques described in §3.2. The fLES32/512, fLES32/1024, ..., fLES32/32768 data can be created by filtering LES64/512, LES64/1024, ..., LES64/32768, respectively, during the recursive process. Table 5 summarizes the present VGMs considered and corresponding training data.

Let us conduct *a priori* and *a posteriori* tests for $Re_L = 375.69$ with $\bar{\Delta}/\eta = 16.76$ (twice that of LES64/256 and LES32/128). During the training process, VGM(128D+256D) employs fDNS data only (fDNS32/128, fDNS64/128 and fDNS32/256), but VGM(128D+256L) utilizes a combination of fDNS and fLES data (fDNS32/128,

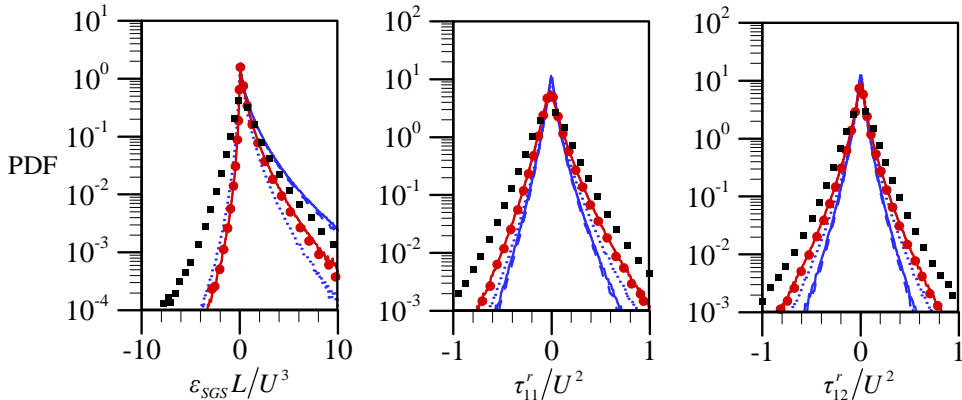


FIGURE 7. Probability density functions (*a priori* test at $Re_L = 375.69$ with $\bar{\Delta}/\eta = 16.76$): (a) SGS dissipation; (b) SGS normal stress; (c) SGS shear stress. \blacksquare , fDNS32/256; \bullet , VGM(128D+256D); --- , VGM(128D+256L); --- , CSM32/256; - - - , DSM32/256; \cdots , GM32/256.

fDNS64/128 and fLES32/256). Table 6 and figure 7 show the results of *a priori* tests. As shown, the performances of VGMs are similar to that of GM, and are better than those of CSM and DSM. A notable observation is that the results of VGM(128D+256L) are nearly identical to those obtained from VGM(128D+256D), implying that fLES data can replace fDNS data in constructing NN-based SGS models. Figures 8 and 9 show the results of energy spectra and PDFs from *a posteriori* tests, respectively, where the result from GM32/256 is not shown because the simulation diverged. Again, VGM(128D+256D) and VGM(128D+256L) perform well among the SGS models considered, but show underpredictions at intermediate wavenumbers. Thus, we perform additional LES with VGM(128D+1024L) whose trained filter sizes are $4.19 \leq \bar{\Delta}_{\text{fDNS}}/\eta$ and $\bar{\Delta}_{\text{fLES}}/\eta \leq 67.02$ (note that the filter sizes for VGM(128D+256L) are $\bar{\Delta}_{\text{fDNS}}/\eta$ and $\bar{\Delta}_{\text{fLES}}/\eta = 4.19 \sim 16.76$). The results with VGM(128D+1024L) are in excellent agreements with fDNS32/256, suggesting that one should expect successful LES when $\bar{\Delta}_{\text{LES}}/\eta$ is within the range of trained filter sizes (see §4.2 for further discussion). It is also notable that the present VGMs do not show the inconsistency between *a priori* and *a posteriori* tests observed from the traditional SGS models (Park *et al.* 2005).

4. Applications to FHIT at high Reynolds numbers and DHIT

To assess the applicability of the present VGMs (table 5), we conduct LESs of FHIT at high Reynolds numbers and of DHIT.

4.1. Forced homogeneous isotropic turbulence at high Reynolds numbers

LESs of FHIT with the number of grid points of 64^3 (LES64/256, LES64/512, LES64/1024, LES64/2048, LES64/4096, LES64/8192, LES64/16384, and LES64/32768) are conducted at eight different Reynolds numbers ($Re_L = 375.69 - 242347.33$) using five different SGS models (VGM128D, VGM(128D+32768L), CSM, DSM, and GM). The computational time step is set at $\Delta t U/L = 0.0025$, at which the Courant–Friedrichs–Lewy (CFL) numbers are below 0.3. Figure 10 shows the three-dimensional energy spectra at eight Reynolds numbers from various SGS models, together with the Kolmogorov energy spectrum. First, LESs with GM reveal instability at high Reynolds numbers. LESs without SGS model exhibit non-physical energy pile

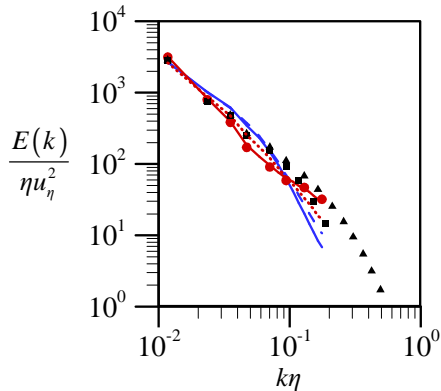


FIGURE 8. Three-dimensional energy spectra (*a posteriori* test at $Re_L = 375.69$ with $\bar{\Delta}_{LES}/\eta = 16.76$): \blacktriangle , DNS256; \blacksquare , fDNS32/256; \bullet , VGM(128D+256D); --- , VGM(128D+256L); \cdots , VGM(128D+1024L); --- , CSM32/256; - - - , DSM32/256.

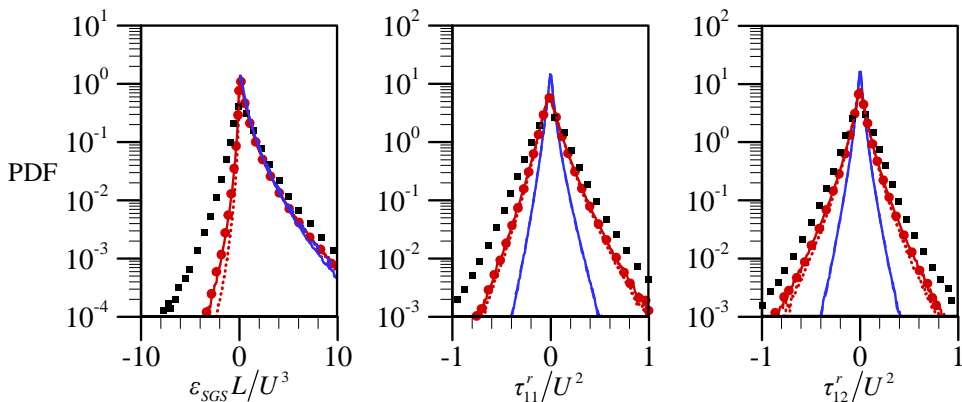


FIGURE 9. Probability density functions (*a posteriori* test at $Re_L = 375.69$ with $\bar{\Delta}_{LES}/\eta = 16.76$): (a) SGS dissipation; (b) SGS normal stress; (c) SGS shear stress. \blacksquare , fDNS32/256; \bullet , VGM(128D+256D); --- , VGM(128D+256L); \cdots , VGM(128D+1024L); --- , CSM32/256; - - - , DSM32/256.

up at high wavenumbers (figure 10(f)) due to insufficient dissipation. A similar pile up of energy at high wavenumbers is also observed in LESs with VGM128D (figure 10(b)). The results from VGM128D indicate an inherent limitation of non-recursive NN-based SGS model, when the LES grid size is bigger than the filter sizes of fDNS employed for training the NN. On the other hand, VGM(128D+32768L) suitably calculates the energy spectra that are quite similar to those of CSM and DSM (figures 10(c) and (d)). The predicted energy spectra from VGM, CSM and DSM follow the Kolmogorov energy spectrum at low and intermediate wavenumbers.

4.2. Decaying homogeneous isotropic turbulence

The present approach is based on a hypothesis that the NN-based SGS models in LES successfully predict the turbulence statistics when the LES grid size normalized by the Kolmogorov length scale is within the range of filter sizes used for training (see also Park & Choi (2021)). In figure 11, we indicate the filter sizes (normalized by the Kolmogorov length scale) used for LESs of FHIT with VGMs and the normalized

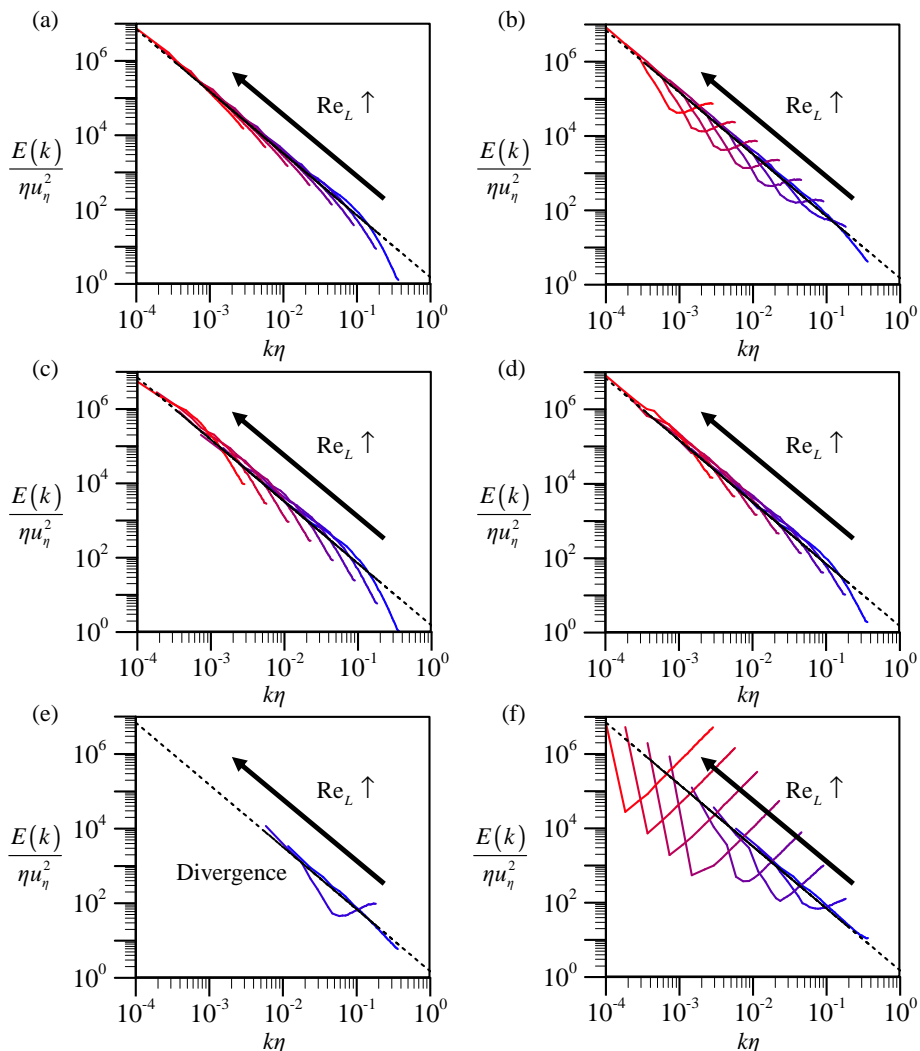


FIGURE 10. Three-dimensional energy spectra at $Re_L = 375.69 - 242347.33$ from various SGS models: (a) VGM(128D+32768L); (b) VGM128D; (c) CSM; (d) DSM; (e) GM; (f) no SGS model. The black dashed line (---) denotes the Kolmogorov energy spectrum, $E(k) = \frac{3}{2}\epsilon^{2/3}k^{-5/3}$.

grid sizes used for promising LESs of two DHITs, respectively. This figure should be understood as follows: for DHIT of Comte-Bellot & Corrsin (1971), VGM(128D+1024L) or VGM(128D+32768L) can be used for successful LES, but not VGM128D and VGM(128D+256L); for DHIT of Kang *et al.* (2003), only VGM(128D+32768L) can be used for successful LES. To examine this hypothesis, LESs are performed for two DHITs of Comte-Bellot & Corrsin (1971) and Kang *et al.* (2003) with the present VGMs trained with FHIT data. This task should be a notable challenge due to transient nature of DHIT as opposed to FHIT.

The first DHIT to simulate is the experiment by Comte-Bellot & Corrsin (1971) (called CBC hereafter). In CBC, turbulence data were experimentally generated through grid turbulence using a mesh size of $M = 5.08$ cm and free-stream velocity of $U_0 = 10$ m/s. The Reynolds number based on the Taylor integral length scale was $Re_\lambda = 71.6$

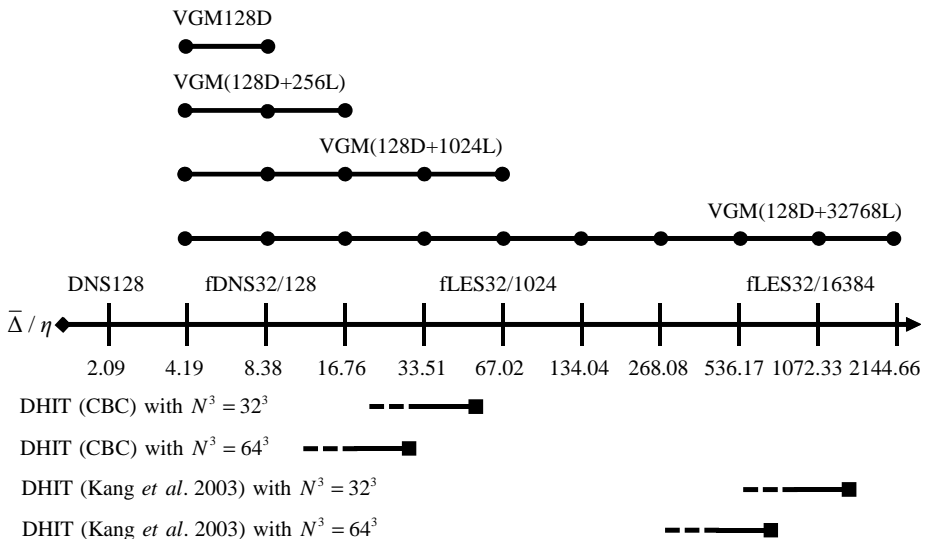


FIGURE 11. Illustration of the filter-size ranges of fDNS and fLES used to generate each VGM (FHIT), and the grid-size ranges required for the simulations of DHITs (Comte-Bellot & Corrsin 1971; Kang *et al.* 2003). On the top of this figure (FHIT), each solid circle (\bullet) denotes the filter size of fDNS or fLES used for generating training data. For each VGM, the line connecting the first and last solid circles indicates the range of grid sizes for successful LES. On the bottom of this figure (DHIT), each solid square (\blacksquare) indicates the grid size normalized by the initial Kolmogorov length scale. As time goes by, the Kolmogorov length scale increases and thus $\bar{\Delta}_{LES}/\eta$ decreases denoted as a thick dashed line.

at $tU_0/M = 42$. For LES, flow variables are non-dimensionalized by $L = 11M/(2\pi)$ and $U = \sqrt{3/2} u_{rms}|_{tU_0/M=42}$ (Lee *et al.* 2010). The numbers of grid points tested are $N^3 = 32^3$ and 64^3 , respectively. A divergence-free initial field is obtained using logistic polynomial approximation method (Knight *et al.* 1998) and rescaling method (Kang *et al.* 2003). LESs are performed 30 times by varying initial fields to obtain ensemble averages. The computational time step is fixed to be $\Delta t U/L = 0.01$. As turbulence decays in time, the Kolmogorov length scale η increases in time, and thus $\bar{\Delta}_{LES}/\eta = 60.2$ and 26.5 ($N^3 = 32^3$), and 30.1 and 13.2 ($N^3 = 64^3$) at $tU_0/M = 42$ and 171 , respectively. Each LES starts from large $\bar{\Delta}_{LES}/\eta$ (denoted as a solid square in figure 11) and moves to smaller $\bar{\Delta}_{LES}/\eta$ due to increased η in time (denoted as a thick dashed line).

The LES results on CBC DHIT with $N^3 = 32^3$ (starting from $\bar{\Delta}_{LES}/\eta = 60.2$) are given in figure 12. Without SGS model, the turbulent kinetic energy decays very slowly and energy pile up occurs at high wavenumbers. With GM, resolved kinetic energy first decreases and increases later in time, and simulation finally diverges, as shown in Vreman *et al.* (1996). DSM and CSM are relatively good at predicting turbulence decay and energy spectra, but they overestimate the energy spectra at intermediate wavenumbers within the inertial range. On the other hand, VGM(128D+32768L) performs best in predicting energy spectra, while VGM(128D+1024L) also performs better than other types of SGS models but shows energy pile up at high wavenumbers, possibly because $\bar{\Delta}_{LES}/\eta$ (≤ 60.2) is only slightly smaller than $\bar{\Delta}_{fLES}/\eta = 67.02$ (fLES32/1024). Note also that the prediction with VGM128D ($\bar{\Delta}_{LES}/\eta \gg \bar{\Delta}_{fDNS}/\eta = 8.38$) is not good at all and worse than CSM and DSM, validating our conjecture on the choice of VGM for successful LES (figure 11). With $N^3 = 64^3$ (starting from $\bar{\Delta}_{LES}/\eta = 30.1$), VGM(128D+1024L) also performs very good as much as VGM(128D+32768L) does (figure 13), because $\bar{\Delta}_{LES}/\eta$ (≤ 30.1)

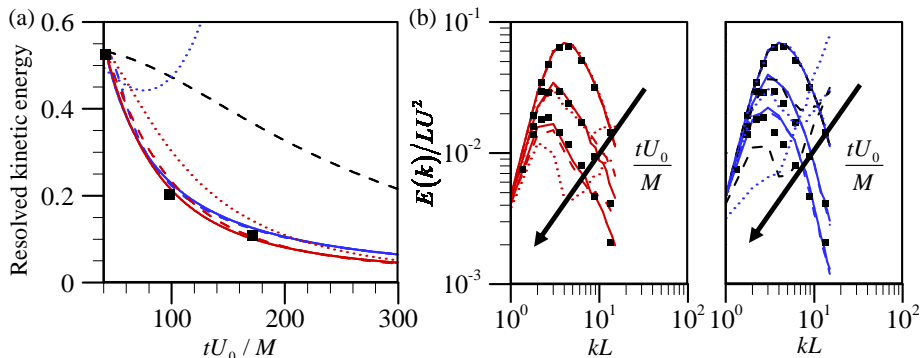


FIGURE 12. LES of CBC DHIT with $N^3 = 32^3$: (a) resolved turbulent kinetic energy; (b) $E(k)$ at $tU_0/M = 42, 98$ and 171 from VGM128D, VGM(128D+1024L), VGM(128D+32768L), CSM, DSM, GM and no SGS model. ■, Filtered CBC data; ·····, VGM128D; - - -, VGM(128D+1024L); —, VGM(128D+32768L); —, CSM; - - -, DSM; ·····, GM; - - -, no SGS model.

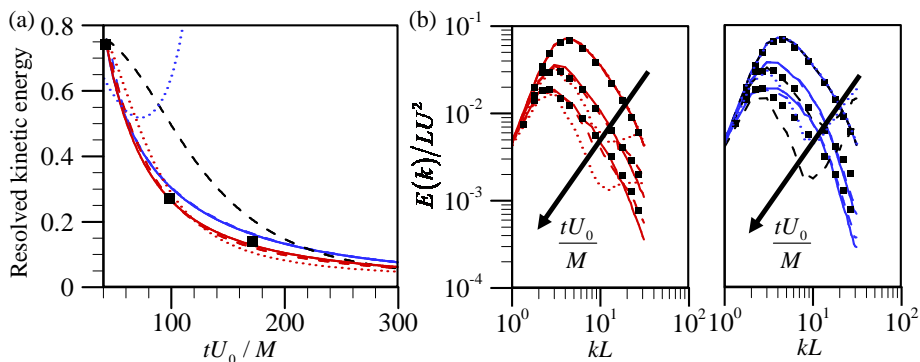


FIGURE 13. LES of CBC DHIT with $N^3 = 64^3$: (a) resolved turbulent kinetic energy; (b) $E(k)$ at $tU_0/M = 42, 98$ and 171 from VGM128D, VGM(128D+1024L), VGM(128D+32768L), CSM, DSM, GM and no SGS model. ■, Filtered CBC data; ·····, VGM128D; - - -, VGM(128D+1024L); —, VGM(128D+32768L); —, CSM; - - -, DSM; ·····, GM; - - -, no-SGS model.

is sufficiently smaller than $\bar{\Delta}_{\text{FLES}}/\eta = 67.02$, while other SGS models still show some deviations from experimental data.

The second DHIT to simulate is the experimental one by Kang *et al.* (2003). The Reynolds number is much higher ($Re_\lambda = 716$ at $tU_0/M = 20$) than that of CBC DHIT, where $U_0 = 11.2$ m/s and $M = 0.152$ m. We examine five SGS models (VGM(128D+32768L), VGM128D, CSM, DSM, and GM), and LESs are performed 30 times by varying initial fields to obtain ensemble averages. The flow variables are non-dimensionalized by $L = 33.68M/(2\pi)$ and $U = \sqrt{3}/2 u_{rms}|_{tU_0/M=20}$. The numbers of grid points tested are $N^3 = 32^3$ and 64^3 , respectively. The flows are initiated using the energy spectrum and rescaling method as done in Kang *et al.* (2003). For $N^3 = 32^3$, $\bar{\Delta}_{\text{LES}}/\eta = 1454.5$ and 888.9 at $tU_0/M = 20$ and 48 , respectively. The trained grid sizes of VGM(128D+32768L) ($4.19 \leq \bar{\Delta}_{\text{FDNS}}/\eta$ and $\bar{\Delta}_{\text{FLES}}/\eta \leq 2144.66$) include this range of $\bar{\Delta}_{\text{LES}}/\eta$, whereas those of VGM128D ($4.19 \leq \bar{\Delta}_{\text{FDNS}}/\eta \leq 8.38$) do not (see figure 11), suggesting that VGM(128D+32768L) should properly predict turbulence decay and variation of the energy spectra of DHIT by Kang *et al.* (2003).

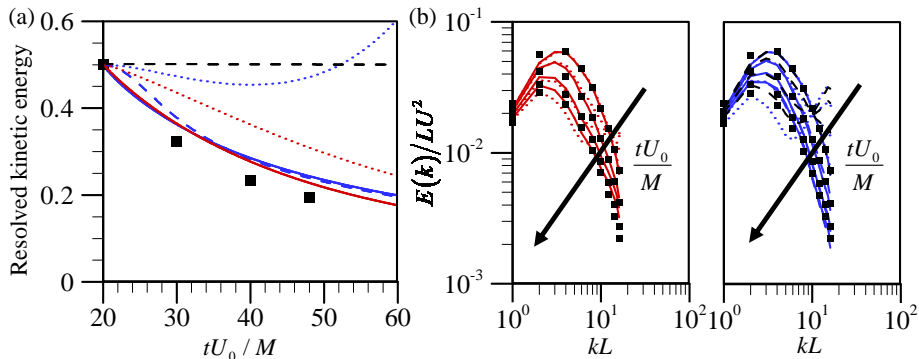


FIGURE 14. LES of DHIT by Kang *et al.* (2003) with $N^3 = 32^3$: (a) resolved turbulent kinetic energy; (b) $E(k)$ at $tU_0/M = 20, 30, 40$ and 48 from VGM128D, VGM(128D+32768L), CSM, DSM, GM and no SGS model. ■, Filtered experimental data; ·····, VGM128D; —, VGM(128D+32768L); —, CSM; - - -, DSM; ·····, GM; - - -, no-SGS model.

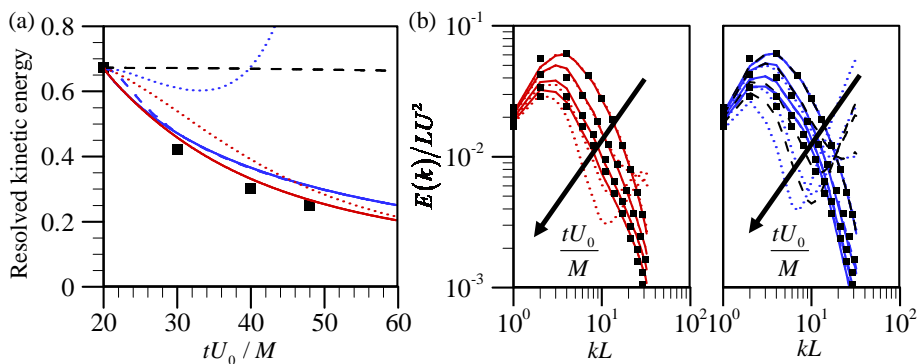


FIGURE 15. LES of DHIT (Kang *et al.* 2003) with $N^3 = 64^3$: (a) resolved turbulent kinetic energy; (b) $E(k)$ at $tU_0/M = 20, 30, 40$ and 48 from CSM, DSM, GM and no SGS model; (c) from VGM128D and VGM(128D+32768L). ■, Filtered experimental data; ·····, VGM128D; —, VGM(128D+32768L); —, CSM; - - -, DSM; ·····, GM; - - -, no-SGS model.

The LES results on DHIT by Kang *et al.* (2003) with $N^3 = 32^3$ are shown in figure 14. While CSM and DSM overpredict the energy spectra even at intermediate wavenumbers and thus overestimate turbulent kinetic energy, VGM(128D+32768L) predicts the resolved kinetic energy and energy spectra most accurately. However, VGM(128D+32768L) shows slight overprediction of energy at high wavenumbers, causing higher resolved kinetic energy than the experimental one. The prediction behaviours of SGS models considered are very similar to what we observed from CBC DHIT. By increasing the number of grid points ($N^3 = 64^3$), the predictions by VGM(128D+32768L) become much better (figure 15). It is interesting to see that the level of kinetic energy without SGS model is almost constant in time due to the energy pile up at high wavenumbers. This is because the LES grid size ($\Delta_{LES}/\eta \approx 10^3$) is so large that the corresponding eddies do not properly dissipate energy at these length scales, and thus total kinetic energy is nearly conserved without SGS model.

5. Conclusions

In the present study, we developed an NN-based SGS model (velocity gradient model; VGM) using a dual NN architecture (the output of one NN is the SGS normal stresses and that of the other is the SGS shear stresses, respectively) with the input of $\bar{\Delta}^2|\bar{\alpha}|_{ij}$, where α_{ij} is the velocity gradient tensor. By eliminating bias and employing the leaky ReLU function as an activation function within the NNs, the present NN retains its nonlinearity but satisfies $\mathbf{NN}(c\mathbf{A}) = c\mathbf{NN}(\mathbf{A})$ for a positive scalar c . This important property of NN allows us to apply the NN to a flow different from the trained one, because the parameters used for non-dimensionalization can be included in the scalar c . To generate training data, we adopted a cut-Gaussian filter rather than the Gaussian or spectral cut-off filter, considering its application to LES with coarser grids and realizability condition, respectively. We also designed a recursive procedure which consisted of the following steps: (1) conducting DNS; (2) training an NN with fDNS data; (3) conducting LES at a higher Reynolds number; (4) training the NN with augmented data including fLES data; (5) going to (3) for higher Reynolds number flows. For the present FHIT, the grid and filter sizes were normalized by the Kolmogorov length scale, and these normalized sizes became double at every recursive procedure. The NN trained through this recursive procedure contained a wide range of filter sizes normalized by the Kolmogorov length scale such that the LES grid size required could be located within this range of filter sizes. Testing VGMs on FHIT showed that fLES data can be a practical alternative to fDNS data for training an NN, and one can avoid using costly DNS to extract training data.

We conducted LESs of forced and decaying homogeneous isotropic turbulence (FHIT and DHIT) with VGMs and traditional SGS models, respectively. In FHIT, the same number of grid points was used for different Reynolds numbers. Among the SGS models considered, VGM constructed through the recursive process performed very well for FHIT. In contrast, VGM trained only with fDNS data at a low Reynolds number showed energy pile up at high wavenumbers. We considered two different DHIT, one by Comte-Bellot & Corrsin (1971) and the other at much higher Reynolds number by Kang *et al.* (2003). In both DHIT, the recursive VGM predicted the decay of resolved turbulent kinetic energy and its energy spectra in time most accurately among the SGS models considered, while other SGS models provided excessive energy spectra at intermediate or high wavenumbers.

In the present study, we applied the VGM to FHIT and DHIT, but this procedure may not be applicable to laminar and inhomogeneous turbulent flows. Hence, the next step is to extend the present approach to those flows by employing dynamic approach used in DSM or training NN with more flows having different topology. This work is being carried out in our group (Kim & Choi 2023; Cho & Choi 2023).

Declaration of Interests. The authors report no conflict of interest.

Acknowledgements This work is supported by the National Research Foundation through the Ministry of Science and ICT (no. 2022R1A2B5B0200158612 and 2021R1A4A1032023). The computing resources are provided by the KISTI Super Computing Center (no. KSC-2023-CRE-0197).

REFERENCES

- ABEKAWA, A., MINAMOTO, Y., OSAWA, K., SHIMAMOTO, H. & TANAHASHI, M. 2023 Exploration of robust machine learning strategy for subgrid scale stress modeling. *Phys. Fluids* **35** (1), 015162.

- ADRIAN, R. 1990 Stochastic estimation of sub-grid scale motions. *Appl. Mech. Rev.* **43**, S214–S218.
- ADRIAN, R. J., JONES, B. G., CHUNG, M. K., HASSAN, Y., NITHIANANDAN, C. K. & TUNG, A. T.-C. 1989 Approximation of turbulent conditional averages by stochastic estimation. *Phys. Fluids A* **1** (6), 992–998.
- BARDINA, J., FERZIGER, J. & REYNOLDS, W. 1980 Improved subgrid-scale models for large-eddy simulation. In *13th fluid and plasmadynamics conference*, p. 1357.
- BECK, A., FLAD, D. & MUNZ, C.-D. 2019 Deep neural networks for data-driven les closure models. *J. Comput. Phys.* **398**, 108910.
- BENGIO, Y., SIMARD, P. & FRASCONI, P. 1994 Learning long-term dependencies with gradient descent is difficult. *IEEE transactions on neural networks* **5** (2), 157–166.
- CHENG, Y., GIOMETTO, M. G., KAUFFMANN, P., LIN, L., CAO, C., ZUPNICK, C., LI, H., LI, Q., HUANG, Y., ABERNATHEY, R. & PIERRE, G. 2022 Deep learning for subgrid-scale turbulence modeling in large-eddy simulations of the convective atmospheric boundary layer. *J. Adv. Model. Earth Syst.* **14** (5), e2021MS002847.
- CHO, C. & CHOI, H. 2023 A dynamic recursive neural-network-based subgrid-scale model for large eddy simulation. In *76th Annual Meeting of the Division of Fluid Dynamics*. Washington D.C., USA.
- CLARK, R. A., FERZIGER, J. H. & REYNOLDS, W. C. 1979 Evaluation of subgrid-scale models using an accurately simulated turbulent flow. *J. Fluid Mech.* **91** (1), 1–16.
- COMTE-BELLOT, G. & CORRISIN, S. 1971 Simple eulerian time correlation of full-and narrow-band velocity signals in grid-generated, ‘isotropic’ turbulence. *J. Fluid Mech.* **48** (2), 273–337.
- DRUMMOND, C. & HOLTE, R. C. 2003 C4. 5, class imbalance, and cost sensitivity: why under-sampling beats over-sampling. In *Workshop on learning from imbalanced datasets II*, , vol. 11, pp. 1–8.
- GAMAHARA, M. & HATTORI, Y. 2017 Searching for turbulence models by artificial neural network. *Phys. Rev. Fluids.* **2**, 054604.
- GERMANO, M., PIOMELLI, U., MOIN, P. & CABOT, W. H. 1991 A dynamic subgrid-scale eddy viscosity model. *Phys. Fluids A* **3** (7), 1760–1765.
- GHOSAL, S., LUND, T. S., MOIN, P. & AKSELVOLL, K. 1995 A dynamic localization model for large-eddy simulation of turbulent flows. *J. Fluid Mech.* **286**, 229–255.
- GOODFELLOW, I., BENGIO, Y. & COURVILLE, A. 2016 *Deep learning*. MIT press.
- GUAN, Y., CHATTOPADHYAY, A., SUBEL, A. & HASSANZADEH, P. 2022 Stable a posteriori les of 2d turbulence using convolutional neural networks: Backscattering analysis and generalization to higher re via transfer learning. *J. Comput. Phys* **458**, 111090.
- GUAN, Y., SUBEL, A., CHATTOPADHYAY, A. & HASSANZADEH, P. 2023 Learning physics-constrained subgrid-scale closures in the small-data regime for stable and accurate les. *Physica D* **443**, 133568.
- HE, K., ZHANG, X., REN, S. & SUN, J. 2016 Deep residual learning for image recognition. In *Proceedings of the IEEE Conference on Computer Vision and Pattern Recognition (CVPR)*.
- IOFFE, S. & SZEGEDY, C. 2015 Batch normalization: Accelerating deep network training by reducing internal covariate shift. In *International conference on machine learning*, pp. 448–456.
- JAMAAT, A. G. T. & HATTORI, B. Y. 2022 Development of subgrid-scale model for LES of Burgers turbulence with large filter size. *Phys. Fluids* **34** (4), 045120.
- KANG, H. S., CHESTER, S. & MENEVEAU, C. 2003 Decaying turbulence in an active-grid-generated flow and comparisons with large-eddy simulation. *J. Fluid Mech.* **480**, 129–160.
- KIM, J., KIM, H., KIM, J. & LEE, C. 2022 Deep reinforcement learning for large-eddy simulation modeling in wall-bounded turbulence. *Phys. Fluids* **34** (10), 105132.
- KIM, M. & CHOI, H. 2023 Large eddy simulation of flow over a circular cylinder using a neural-network-based subgrid-scale model and its application to complex turbulent flows. In *76th Annual Meeting of the Division of Fluid Dynamics*. Washington D.C., USA.
- KIM, M., PARK, J. & CHOI, H. 2023 Large eddy simulation of flow over a circular cylinder with a neural-network-based subgrid-scale model. Under review.
- KINGMA, D. P. & BA, J. 2014 Adam: A method for stochastic optimization. arXiv:1412.6980.

- KNIGHT, D., ZHOU, G., OKONG’O, N. & SHUKLA, V. 1998 Compressible large eddy simulation using unstructured grids. In *36th AIAA Aerospace Sciences Meeting and Exhibit*, p. 535.
- KRIZHEVSKY, A., SUTSKEVER, I. & HINTON, G. E. 2012 Imagenet classification with deep convolutional neural networks. In *Advances in Neural Information Processing Systems*, , vol. 25, pp. 1097–1105.
- KURZ, M., OFFENHÄUSER, P. & BECK, A. 2023 Deep reinforcement learning for turbulence modeling in large eddy simulations. *Int. J. Heat Fluid Flow* **99**, 109094.
- LANGFORD, J. A. & MOSER, R. D. 1999 Optimal les formulations for isotropic turbulence. *J. Fluid Mech.* **398**, 321–346.
- LEE, J., CHOI, H. & PARK, N. 2010 Dynamic global model for large eddy simulation of transient flow. *Phys. Fluids* **22** (7), 075106.
- LILLY, D. K. 1992 A proposed modification of the germano subgrid-scale closure method. *Phys. Fluids A* **4** (3), 633–635.
- LIU, B., YU, H., HUANG, H., LIU, N. & LU, X. 2022 Investigation of nonlocal data-driven methods for subgrid-scale stress modeling in large eddy simulation. *AIP Advances* **12** (6), 065129.
- LIU, S., MENEVEAU, C. & KATZ, J. 1994 On the properties of similarity subgrid-scale models as deduced from measurements in a turbulent jet. *J. Fluid Mech.* **275**, 83–119.
- LIU, W., QI, H., SHI, H., YU, C. & LI, X. 2023 Helical model based on artificial neural network for large eddy simulation of compressible wall-bounded turbulent flows. *Phys. Fluids* **35** (4), 045120.
- LIU, X. Y., WU, J. & ZHOU, Z. H. 2008 Exploratory undersampling for class-imbalance learning. *IEEE Transactions on Systems, Man, and Cybernetics, Part B (Cybernetics)* **39** (2), 539–550.
- MAAS, A. L., HANNUN, A. Y. & NG, A. Y. 2013 Rectifier nonlinearities improve neural network acoustic models. In *Proc. icml*, , vol. 30, p. 3.
- MACART, J. F., SIRIGNANO, J. & FREUND, J. B. 2021 Embedded training of neural-network subgrid-scale turbulence models. *Phys. Rev. Fluids* **6**, 050502.
- MAULIK, R. & SAN, O. 2017 A neural network approach for the blind deconvolution of turbulent flows. *J. Fluid Mech.* **831**, 151–181.
- MAULIK, R., SAN, O., RASHEED, A. & VEDULA, P. 2018 Data-driven deconvolution for large eddy simulations of Kraichnan turbulence. *Phys. Fluids* **30** (12).
- MAULIK, R., SAN, O., RASHEED, A. & VEDULA, P. 2019 Subgrid modelling for two-dimensional turbulence using neural networks. *J. Fluid Mech.* **858**, 122–144.
- MENEVEAU, C. & KATZ, J. 2000 Scale-invariance and turbulence models for large-eddy simulation. *Annu. Rev. Fluid. Mech* **32** (1), 1–32.
- MOSER, R. D., MALAYA, N. P., CHANG, H., ZANDONADE, P. S., VEDULA, P., BHATTACHARYA, A. & HASELBACHER, A. 2009 Theoretically based optimal large-eddy simulation. *Phys. Fluids* **21** (10).
- NICOUD, F. & DUCROS, F. 1999 Subgrid-scale stress modelling based on the square of the velocity gradient tensor. *Flow Turbul. Combust* **62** (3), 183–200.
- NOVATI, G., DE LAROUSSILHE, H. L. & KOUMOUTSAKOS, P. 2021 Automating turbulence modelling by multi-agent reinforcement learning. *Nat. Mach. Intell.* **3** (1), 87–96.
- PARK, J. & CHOI, H. 2021 Toward neural-network-based large eddy simulation: application to turbulent channel flow. *J. Fluid Mech.* **914**, A16.
- PARK, N., LEE, S., LEE, J. & CHOI, H. 2006 A dynamic subgrid-scale eddy viscosity model with a global model coefficient. *Phys. Fluids* **18** (12), 125109.
- PARK, N., YOO, J. Y. & CHOI, H. 2005 Toward improved consistency of a priori tests with a posteriori tests in large eddy simulation. *Phys. Fluids* **17** (01), 015103.
- PAWAR, S., SAN, O., RASHEED, A. & VEDULA, P. 2020 A priori analysis on deep learning of subgrid-scale parameterizations for kraichnan turbulence. *Theor Comput Fluid Dyn* **34**, 429–455.
- PAWAR, S., SAN, O., RASHEED, A. & VEDULA, P. 2023 Frame invariant neural network closures for kraichnan turbulence. *Physica A: Statistical Mechanics and its Applications* **609**, 128327.
- POPE, S. B. 2000 *Turbulent flows*. Cambridge university press.
- PRAKASH, A., JANSEN, K. E. & EVANS, J. A. 2022 Invariant data-driven subgrid stress

- modeling in the strain-rate eigenframe for large eddy simulation. *Comput. Methods Appl. Mech. Eng.* **399**, 115457.
- PRAT, A., SAUTORY, T. & NAVARRO-MARTINEZ, S. 2020 A priori sub-grid modelling using artificial neural networks. *International Journal of Computational Fluid Dynamics* **34** (6), 397–417.
- ROSALES, C. & MENEVEAU, C. 2005 Linear forcing in numerical simulations of isotropic turbulence: Physical space implementations and convergence properties. *Physics of Fluids* **17** (9), 095106.
- SALVETTI, M. V. & BANERJEE, S. 1995 A priori tests of a new dynamic subgrid-scale model for finite-difference large-eddy simulations. *Phys. Fluids* **7** (11), 2831–2847.
- SARGHINI, F., DE FELICE, G. & SANTINI, S. 2003 Neural networks based subgrid scale modeling in large eddy simulations. *Comput. Fluids* **32** (1), 97–108.
- SILVER, D., HUANG, A., MADDISON, C. J., GUEZ, A., SIFRE, L., VAN DEN DRIESSCHE, G., SCHRITTWIESER, J., ANTONOGLU, I., PANNEERSHELVAM, V., LANCTOT, M., DIELEMAN, S., GREWE, D., NHAM, J., KALCHBRENNER, N., SUTSKEVER, I., LILICRAP, T., LEACH, M., KAVUKCUOGLU, K., GRAEPEL, T. & HASSABIS, D. 2016 Mastering the game of go with deep neural networks and tree search. *Nature* **529** (7587), 484–489.
- SIMONYAN, K. & ZISSERMAN, A. 2014 Very deep convolutional networks for large-scale image recognition. arXiv:1409.1556.
- SIRIGNANO, J. & MACART, J. F. 2023 Deep learning closure models for large-eddy simulation of flows around bluff bodies. *J. Fluid Mech.* **966**, A26.
- SIRIGNANO, J., MACART, J. F. & FREUND, J. B. 2020 Dpm: A deep learning pde augmentation method with application to large-eddy simulation. *J. Comput. Phys.* **423**, 109811.
- SMAGORINSKY, J. 1963 General circulation experiments with the primitive equations: I. the basic experiment. *Mon. Weather. Rev.* **91** (3), 99–164.
- STOFFER, R., VAN LEEUWEN, C. M., PODAREANU, D., CODREANU, V., VEERMAN, M. A., JANSSENS, M., HARTOGENSIS, O. K. & VAN HEERWAARDEN, C. C. 2021 Development of a large-eddy simulation subgrid model based on artificial neural networks: a case study of turbulent channel flow. *Geosci. Model. Dev.* **14**, 3769–3788.
- SUBEL, A., CHATTOPADHYAY, A., GUAN, Y. & HASSANZADEH, P. 2021 Data-driven subgrid-scale modeling of forced Burgers turbulence using deep learning with generalization to higher Reynolds numbers via transfer learning. *Phys. Fluids* **33** (3), 031702.
- VÖLKER, S., MOSER, R. D. & VENUGOPAL, P. 2002 Optimal large eddy simulation of turbulent channel flow based on direct numerical simulation statistical data. *Phys. Fluids* **14** (10), 3675–3691.
- VREMAN, A. W. 2004 An eddy-viscosity subgrid-scale model for turbulent shear flow: Algebraic theory and applications. *Phys. Fluids* **16** (10), 3670–3681.
- VREMAN, B., GEURTS, B. & KUERTEN, H. 1994 Realizability conditions for the turbulent stress tensor in large-eddy simulation. *J. Fluid Mech.* **278**, 351–362.
- VREMAN, B., GEURTS, B. & KUERTEN, H. 1996 Large-eddy simulation of the temporal mixing layer using the clark model. *Theor. Comput. Fluid. Dyn.* **8** (4), 309–324.
- VREMAN, B., GEURTS, B. & KUERTEN, H. 1997 Large-eddy simulation of the turbulent mixing layer. *J. Fluid Mech.* **339**, 357–390.
- WANG, Y., YUAN, Z., XIE, C. & WANG, J. 2021 Artificial neural network-based spatial gradient models for large-eddy simulation of turbulence. *AIP Advances* **11** (5), 055216.
- WANG, Z., LUO, K., LI, D., TAN, J. & FAN, J. 2018 Investigations of data-driven closure for subgrid-scale stress in large-eddy simulation. *Phys. Fluids* **30** (12).
- WOLLBLAD, C. & DAVIDSON, L. 2008 Pod based reconstruction of subgrid stresses for wall bounded flows using neural networks. *Flow Turbul. Combust.* **81**, 77–96.
- XIE, C., WANG, J., LI, H., WAN, M. & CHEN, S. 2019a Artificial neural network mixed model for large eddy simulation of compressible isotropic turbulence. *Phys. Fluids* **31** (8).
- XIE, C., WANG, J., LI, H., WAN, M. & CHEN, S. 2020a Spatial artificial neural network model for subgrid-scale stress and heat flux of compressible turbulence. *Theor. Appl. Mech. Lett.* **10** (1), 27–32.
- XIE, C., WANG, J., LI, H., WAN, M. & CHEN, S. 2020b Spatially multi-scale artificial neural network model for large eddy simulation of compressible isotropic turbulence. *AIP Advances* **10**, 015044.

- XIE, C., WANG, J., LI, K. & MA, C. 2019*b* Artificial neural network approach to large-eddy simulation of compressible isotropic turbulence. *Phys. Rev. E* **99**, 053113.
- XIE, C., WANG, J. & WEINAN, E. 2020*c* Modeling subgrid-scale forces by spatial artificial neural networks in large eddy simulation of turbulence. *Phys. Rev. Fluids* **5**, 054606.
- XIE, C., YUAN, Z. & WANG, J. 2020*d* Artificial neural network-based nonlinear algebraic models for large eddy simulation of turbulence. *Phys. Fluids* **32**, 115101.
- XU, B., WANG, N., CHEN, T. & LI, M 2015 Empirical evaluation of rectified activations in convolutional network. arXiv:1505.00853.
- YU, C., YUAN, Z., QI, H., WANG, J., LI, X. & CHEN, S. 2022 Kinetic-energy-flux-constrained model using an artificial neural network for large-eddy simulation of compressible wall-bounded turbulence. *J. Fluid Mech.* **932**, A23.
- YUAN, Z., XIE, C. & WANG, J. 2020 Deconvolutional artificial neural network models for large eddy simulation of turbulence. *Phys. Fluids* **32** (11), 115106.
- ZANNA, L. & BOLTON, T. 2020 Data-driven equation discovery of ocean mesoscale closures. *Geophys Res Lett* **47** (17), e2020GL088376.
- ZHOU, Z., HE, G., WANG, S. & JIN, G. 2019 Subgrid-scale model for large-eddy simulation of isotropic turbulent flows using an artificial neural network. *Comput. Fluids.* **195**, 104319.